RESEARCH ARTICLE
SPACE PHYSICS: MAGNETOSPHERIC PHYSICS

Earth and Planetary Physics
8: 204–214, 2024
doi: 10.26464/epp2023088

Tomographic reconstruction of the Earth's magnetosheath from multiple spacecraft: a theoretical study

A. M. Jorgensen[1], TianRan Sun[2*], Y. Huang[2], L. Li[3], R. Xu[2], L. Dai[2], and Chi Wang[2]

[1]New Mexico Institute of Mining and Technology, Socorro, NM, USA;

[2]National Space Science Center, Chinese Academy of Sciences, Beijing 100190, China;

[3]Tsinghua University, Beijing 100084, China

Key Points:

- Instantaneous reconstruction of the location of the subsolar magnetopause is possible with two soft X-ray imaging satellites.
- Instantaneous reconstruction of a wider section of the magnetosheath is possible with three or more imaging satellites.
- Images that do not contain the boundary nearly edge-on do not contribute meaningfully to boundary reconstruction.

Citation: Jorgensen, A. M., Sun, T. R., Huang, Y., Li, L., Xu, R., Dai, L., and Wang, C. (2024). Tomographic reconstruction of the Earth's magnetosheath from multiple spacecraft: a theoretical study. *Earth Planet. Phys.*, *8*(1), 204–214. http://doi.org/10.26464/epp2023088

Abstract: Following our earlier work on tomographic reconstruction of the magnetosheath soft X-ray emissions with superposed epoch analysis of many images recorded from a single spacecraft we now explore the instantaneous reconstruction of the magnetosheath and magnetopause using a few images recorded simultaneously from a few spacecraft. This work is motivated by the prospect of possibly having two or three soft X-ray imagers in space in the coming years, and that many phenomena which occur at the magnetopause boundary, such as reconnection events and pressure pulse responses, do not lend themselves as well to superposed epoch analysis. If the reconstruction is successful — which we demonstrate in this paper that it can be — this collection of imagers can be used to reconstruct the magnetosheath and magnetopause from a single image from each spacecraft, allowing for high time resolution reconstructions. In this paper we explore the reconstruction using, two, three, and four spacecraft. We show that the location of the subsolar point of the magnetopause can be determined with just two satellites, and that volume emissions of soft X-rays, and the shape of the boundary, can be reconstructed using three or more satellites.

Keywords: magnetosheath; tomography; soft X-ray imaging; SMILE

1. Introduction

Remote sensing, and imaging in particular, is becoming an increasingly valuable tool in measuring space plasmas, dating back nearly 100 years to the ground-based auroral triangulation experiments of Størmer (1935), to the analysis by Akasofu (1964) of auroral images to understand the substorm evolution. Then came space-based imaging of the aurora at different wavelengths, from numerous different spacecraft, and coordinated ground-based and space-based remote sensing observations (e.g., Brittnacher et al., 1997; Mende et al., 2008). In addition to photon emissions from the aurora many other types of radiation have been observed, including Energetic Neutral Atom (ENA) emissions (Roelof et al., 1985; Henderson et al., 1997, 1999; Jorgensen et al., 2000; C:son Brandt et al., 2002; Vallat et al., 2004), particularly from the ring current, and Extreme Ultraviolet (EUV) emissions from the plasmasphere, which are actually sunlight scattered off of singly-ionized helium in the Earth's plasmasphere (Sandel et al., 2001; He H et al., 2016).

Our first step in analyzing soft X-ray emissions consisted of various fitting approaches to volume emissions or to boundaries determined in the images (Jorgensen et al., 2019; Sun TR et al., 2020, 2021). The next step, following the example of Huang Y et al. (2021), was to investigate superposed epoch tomographic reconstruction of the magnetosheath using modeled observations from the Solar Wind Magnetosphere Ionosphere Link Explorer (SMILE) satellite (Wang C et al., 2017; Branduardi-Raymont et al., 2018). This work is detailed in Jorgensen et al. (2022), and a summary can also be found in Wang C and Sun TR (2022). We found that while the reconstruction is possible, and in some cases very good, some artifacts appear in the reconstructions. Naturally, carrying out reliable tomographic reconstructions requires images from different vantage points. This means that instantaneous reconstruction is not possible with data from just one satellite. Using images spread over one orbit of SMILE is barely enough for a reconstruction, one that is likely to have significant artifacts. Reconstruction using images spread over an entire year yields a much better result with fewer artifacts in the reconstruction because of the larger range of

First author: A. M. Jorgensen, Anders.M.Jorgensen@nmt.edu
Correspondence to: T. R. Sun, trsun@swl.ac.cn
Received 05 DEC 2023; Accepted 27 DEC 2023.
First Published online 05 JAN 2024.
©2024 by Earth and Planetary Physics.

viewing angles created by the orbit precession in the Sun–Earth aligned coordinate system which organizes the magnetosphere. However, instantaneous reconstruction remains desirable because many phenomena on the magnetosheath boundaries exist on short characteristic timescales (Sun TR et al., 2015, 2019). Instantaneous reconstruction requires multiple spacecraft.

The present paper is motivated by the prospect of having multiple soft X-ray imaging instruments in space at the same time. The ESA/CAS SMILE mission satellite is currently expected to be launched in 2025. It will be in a highly elliptical orbit which takes it to approximately $20\,R_E$ above the Earth's northern hemisphere. The soft X-ray imager (SXI) on SMILE will have a field-of-view (FOV) of 27 degrees in the dawn–dusk direction by 16 degrees in the noon-midnight direction, with a resolution of 8 arcminutes full-width at half maximum (FWHM). The GEOspace X-ray imager (GEO-X) (Ezoe et al., 2023) is a miniaturized instrument on a CubeSat equipped with a kick-motor which will launch it into a 30 to 60 R_E orbit. The instrument has a FOV of 5 degrees by 5 degrees, a resolution of 10 arcminutes, and energy range from 0.3 to 2 keV. The GEO-X team aims for a launch around the maximum of solar cycle 25, overlapping with SMILE. The recent increase in activity on the Moon by at least the US and Chinese space agencies presents opportunities to propose additional instruments. The Lunar Environment Heliospheric X-ray Imager (LEXI) is a lunar surface soft X-ray imager that will be launched as part of NASA's Lunar Surface Instrument and Technology Payloads (LSITP) program. LEXI will have a field of view of 9.1 by 9.1 degrees (Paw et al., 2022), a resolution of 0.2 degrees, and energy coverage from 0.2 to 4.0 keV. Due to the harsh environment on the Moon, LEXI is expected to operate for one lunar day after landing, and not survive the following lunar night. The Lunar-based Soft X-ray Imager (LSXI) (Guo YH et al., 2021) is a concept for a soft X-ray imager on the Moon, potentially as part of a Chinese Lunar lander mission. The LSXI is designed to have a FOV of 15 degrees (in the day-night direction) by 30 degrees (in the north-south direction), a resolution of 10 arcminutes, and energy coverage from 200 eV to 2.5 keV. The Solar-Terrestrial Observer for the Response of the Magnetosphere (STORM) (Sibeck et al., 2023) is a single-spacecraft mission which has conducted an extensive Phase A study for NASA, but which has not yet been selected for implementation. STORM is designed to observe the solar wind plasma and magnetic field input in situ, and the response of key magnetospheric plasma structures remotely, via a suite of telescopes including a soft X-ray imager. Following a single lunar assist, the STORM satellite is designed to fly in a circular polar orbit with a radius of approximately $30\,R_E$. Based on this mixture of actual planned missions and possible future missions, we model some imaging scenarios involving from two to four spacecraft instruments, some of which correspond to SMILE SXI-like instruments in SMILE-like, STORM-like, or Moon-like orbits. From combinations of simulated versions of those images we reconstruct the magnetosheath tomographically, and examine the quality of the reconstructions, using the computed tomography (CT) methods that we used previously (Jorgensen et al., 2022). In the sections below, methods are only briefly summarized; readers may find additional methodological detail in the papers cited in each section.

2. Methodology

The approach we take is simulate the 3D soft X-ray emissions from the magnetosheath (Section 2.1), generate simulated images of those emissions (Section 2.2), use those images in tomographic reconstructions (Section 2.3), and then compare the reconstructions to the simulated 3D emissions with which we started (Section 3).

2.1 Emissions Model

Soft X-ray emissions are the result of charge-exchange reactions between highly ionized solar wind ions and the cold atoms of the Earth's extended atmosphere, also known as the geocorona. Solar wind plasma is a necessary component of this interaction because the energy of electron decay into a deep-energy orbital of the highly ionized ions lies in the soft X-ray regime. A representative, important reaction is

$$O^{7+} + H = O^{6+} + H^{+} + \gamma, \tag{1}$$

but other charge states and species are also involved, among which the emissions from C and N ions are expected to dominate. Tab. 1 of Schwadron and Cravens (2000) states that for fast solar wind the dominant species (>3%) are C^{6+}, C^{5+}, N^{5+}, N^{6+}, O^{6+}, O^{7+}, Ne^{8+}, and Si^{9+}. Of those, O^{7+} has the highest energy, 709 eV, and can be distinguished as a separate line in the SXI spectrogram, O^{6+}, the most abundant (Owens et al., 2018), has an energy, 103 eV, that is below the SXI lower band edge of 200 eV. The remaining lines, are either below the energy threshold, or are likely not distinguishable as individual lines. For slow solar wind the composition changes somewhat, including greater abundance of the higher charge state oxygen ions. Carter et al. (2010) shows an observation from XMM-Newton in which changing composition is used to identify a passing coronal mass ejection that was observed also by solar wind monitors.

Soft X-ray photons can be observed with an appropriate camera. For imaging purposes with the SMILE SXI, the plan is to integrate the SXI spectrum from 200 eV to 1000 eV in order to maximize the signal-to-noise ratio (SNR) of the images. Because the emissions come only from outside the magnetosphere, the images from appropriate vantage points will contain a sharp boundary, which is a signature of the magnetopause. We model these emissions starting with the output of a magnetohydrodynamic model, the PPMLR-MHD (Hu YQ et al., 2007) which outputs plasma density. We use the same model run as is used in Jorgensen et al. (2022), with solar wind parameters $n_{sw} = 35\,\mathrm{cm^{-3}}$, $v_{sw} = 400\,\mathrm{km/s}$, and IMF $B_z = -5\,\mathrm{nT}$. For additional information about the model run we refer the reader to Jorgensen et al. (2022). From the MHD model output, the X-ray emission rate can be computed according to

$$P = a_{cx} n_H n_{sw} \langle g \rangle, \tag{2}$$

where P is in $\mathrm{eV\,cm^{-3}\,s^{-1}}$, n_H is the geocorona density, n_{sw} is the solar wind number density. a_{cx} is an efficiency factor that sums over all species and all transitions. a_{cx} can be defined as

$$a_{cx} = \sum_s f_s \sum_q f_{sq} \sigma_{sq} \sum_j f_{sqj} \Delta E_{sqj}, \tag{3}$$

where s indexes the solar wind heavy ion species, q is the charge state, and j the transition. Then f_s is the fraction of the solar wind

ion density, n_{sw}, that is of species s; f_{sq} is the fraction of those that are in charge-state q; f_{sqj} is the transition j probability of those, multiplied by the instrumental response; and ΔE_{sqj} is the energy released in the transition. $\langle g \rangle = \sqrt{u_{sw}^2 + u_{th}^2}$ is the collision speed, which is the geometric mean of the bulk velocity and the thermal velocity. For additional discussion the reader is referred to Cravens (2000). Figure 1 shows the resulting computed soft X-ray emission. Panel a shows an equatorial cut (XY plane for $Z = 0$) through the emission; panel b shows a meridional cut (XZ plane for $Y = 0$). The emission is more intense closer to the Earth where the geocoronal density is greater, but drops to zero inside the magnetopause, beyond which no solar wind penetrates, and thus no highly ionized ions are there. The magnetopause is visible as the boundary between the high emissions of the magnetosheath, and the zero emissions inside the magnetosphere. The bow shock can also be seen. After the bow shock, the plasma is hotter and denser, which results in a greater volume emission from the magnetosheath region.

2.2 Simulated Soft X-ray Images

From the volume emissions we generate simulated intensity images by integrating through the volume along the line-of-sight of each pixel,

$$I = \frac{1}{4\pi} \int P \, \mathrm{d}l, \tag{4}$$

where I is in $\mathrm{eV\,cm^{-2}\,s^{-1}\,sr^{-1}}$. The intensity images can then be used to generate average photon count images by multiplying by the geometric factor of each pixel and by the integration time. However for the purposes of this paper the intensity image is sufficient and we will proceed with it. We use the nominal SMILE field-of-view of 16 degrees along the short dimension and 27 degrees along the long dimension, with 113 pixels along the short dimension and 194 along the long dimension. This results in a resolution of approximately 8 arcminutes which is close to the expected resolution of the SMILE SXI imager. Figure 2 shows the six images that we will use for the reconstructions in this paper. These images were chosen to allow for reconstructions using 2, 3, and 4 images, and demonstrating also the effect of imaging vantage point. In the rest of the paper we refer to their images according to the panel labels, a to f. All images point toward the nominal subsolar location of the magnetopause, $(x, y, z) = (7, 0, 0)\,R_E$. Image a is for a vantage point $(x, y, z) = (5, 5, 20)$ above the north pole, corresponding approximately to a point on a SMILE-like orbit. Images b and c are for vantage points $(x, y, z) = (5, 25, 5)$ and $(x, y, z) = (5, -25, 5)$, respectively, corresponding to points on a STORM-like orbit, approximately at dusk and dawn, respectively. Image d is for a vantage point $(x, y, z) = (55, 10, -5)$, corresponding approximately to the location of the New Moon. Images e and f, at $(x, y, z) = (25, 25, 9)$ and $(x, y, z) = (17, 17, 17)$ are two locations on the afternoon side at different latitudes, but are not intended to correspond to one of the three anticipated future imagers; they are used only in the four-satellite reconstruction.

2.3 Tomographic Reconstruction

For the reconstruction, we use the Algebraic Reconstruction Technique (ART) (Gordon et al., 1970), which is one of the oldest, and simplest tomographic reconstruction techniques. In a discrete reconstruction problem, with images consisting of pixels, and a reconstruction volume consisting of a finite number of discrete

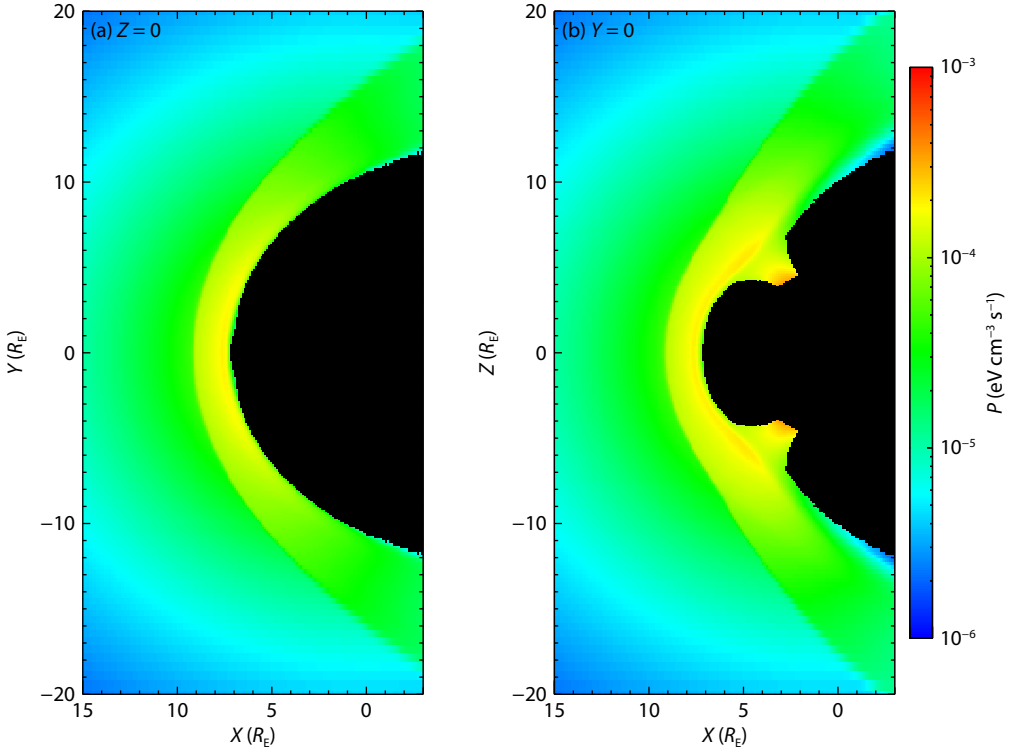

Figure 1. Meridional (left) and equatorial (right) cut through the soft X-ray emission model used in this paper. See text for details on how it was computed.

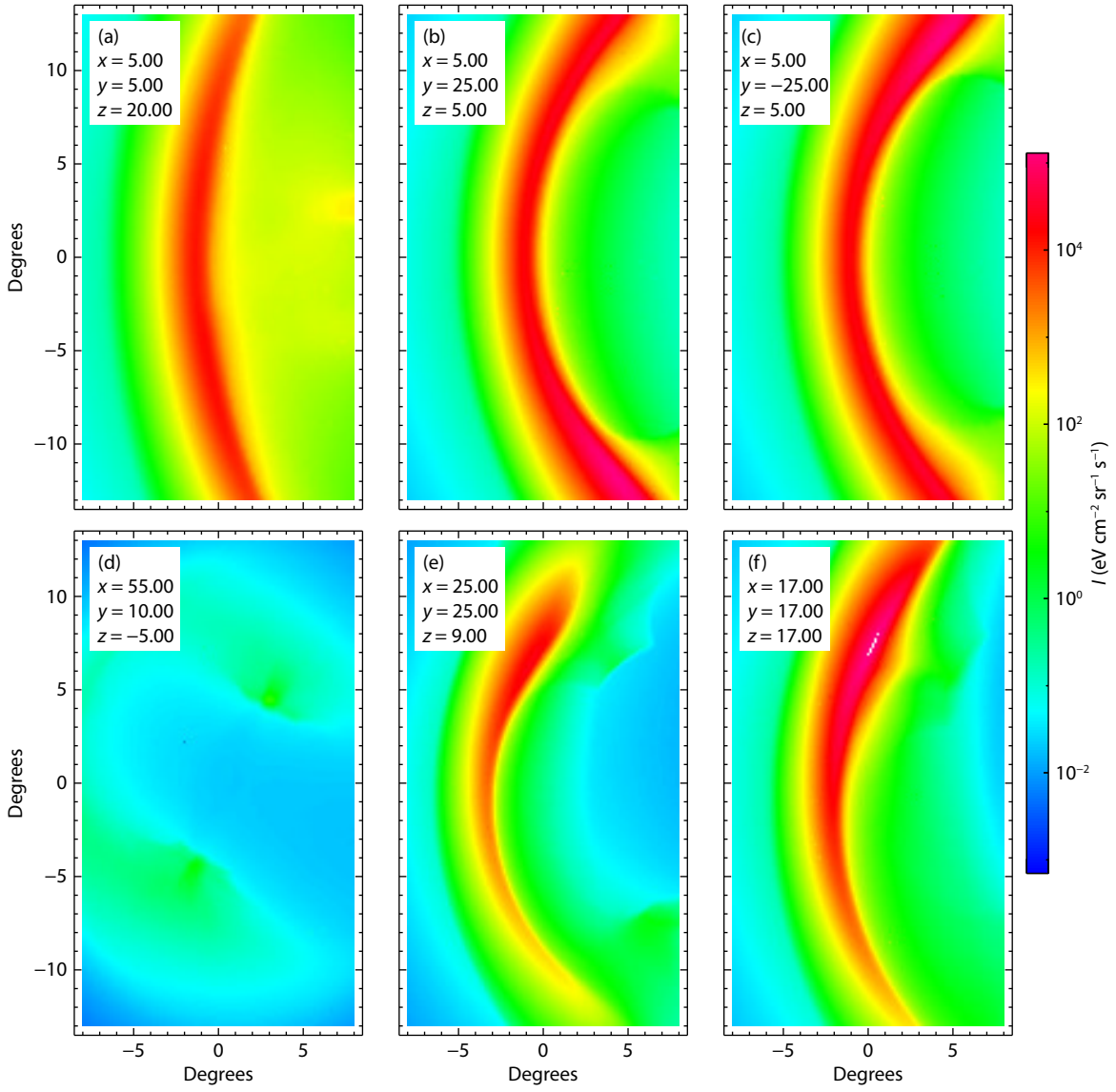

Figure 2. The six images that are used in various combinations for the tomographic reconstructions. Each image has a field-of-view of 16 degrees in the short dimension by 27 degrees in the long dimension (113 pixels in the short dimension by 194 in the long dimension). The panel labels a–f are used in the paper to refer to these images. The coordinates written in the images give the location of the camera, in each case pointing from that location to $(x, y, z) = (7, 0, 0)\ R_E$.

cells, the reconstruction problem can be represented as a matrix equation,

$$\bar{\bar{\boldsymbol{A}}}\bar{\boldsymbol{u}} = \bar{\boldsymbol{p}}. \tag{5}$$

Here $\bar{\boldsymbol{u}}$, which is a column vector of length n, represents the volume elements; and $\bar{\boldsymbol{p}}$, which is a column vector of length m, represents all the pixels in all the images. The matrix $\bar{\bar{\boldsymbol{A}}}$, which has dimensions m rows of n columns, is a geometry matrix that represents the weights. Thus, pixel i in $\bar{\boldsymbol{p}}$, is modeled as this sum,

$$p_i = \sum_{j=1}^{n} A_{ij} u_j, \tag{6}$$

where A_{ij} is the weight of volume element j in the irradiance on pixel i. Typically A_{ij} will be proportional to the distance spent by ray i in volume element j. The tomographic problem then consists of the inverse problem, determining $\bar{\boldsymbol{u}}$ given $\bar{\boldsymbol{p}}$, when $\bar{\bar{\boldsymbol{A}}}$ is known. $\bar{\boldsymbol{u}}$ may have many more elements than $\bar{\boldsymbol{p}}$, which makes the problem ill-posed without additional constraints. The ART algorithm implicitly imposes a smoothness constraint, such that, in the absence of constraints from other pixels, the emission from a pixel will be distributed uniformly along the pixel ray path. That is why tomographic reconstructions using the ART algorithm sometimes contain streaks that are aligned with the ray paths. That can happen when there is not enough information in the data to determine where along the ray path the emissions should be placed, or when there is inconsistency between crossing ray paths. The ART algorithm iteratively seeks to adjust the volume element emissions in order to minimize, in the aggregate, the difference between image pixels and the corresponding sums in Equation (6). One sub-iteration consists of adjusting some of the elements in the vector $\bar{\boldsymbol{u}}$, specifically the elements for which the elements in $\bar{\bar{\boldsymbol{A}}}$ are non-zero. One iteration is completed after a sub-

iteration is completed for every pixel, as shown in Equation (7).

$$\bar{u}^{k+1,i} = \bar{u}^{k,i-1} + \lambda_k \frac{p_i - \bar{A}_i \cdot \bar{u}^k}{||\bar{A}_i||^2} \bar{A}_i^{\mathrm{T}}. \quad (7)$$

For $i = 1$, $u^{k,i-1}$ is replaced with $u^{k-1,i}$. The order in which the pixels are used is normally random. Although the ART algorithm imposes a smoothness criterion, we have found that an additional criterion should be applied for best results. Approximately every several iterations of the ART algorithm, we use a total variation denoising technique (Rudin et al., 1992), which here is image denoising. For more details of how this algorithm is implemented the reader is referred to Chambolle (2004), as well as to our earlier paper. In addition to the theoretical work by Huang Y et al. (2021), which inspired the present work, tomographic reconstruction has also been applied to real space plasma observations, including those of Gustavsson (1998) and Aso et al. (1998).

3. Results

We simulate six images, shown in Figure 2, and use different numbers and combinations of these images to create tomographic reconstructions. All six images cover a field of view of 16 degrees in the short dimension by 27 degrees in the long dimension (113 pixels in the short direction and 194 pixels in the long direction). In the following sections we refer to these images by their panel labels, a to f. In each of the reconstruction experiments, which we label case A through case E, we use the same reconstruction volume; its size is $20\,R_E$ along each dimension with volume elements of $0.125\,R_E$ in each dimension. The X-dimension goes from $-3\,R_E$ while the Y and Z dimensions are centered around the origin.

3.1 Two Satellites

Figure 3 presents results of the first experiment (case A) in which we examine a reconstruction based on images a and b from two satellites located, respectively, at $(x, y, z) = (5, 5, 20)\,R_E$ (which is similar to apogee in a SMILE orbit), and $(x, y, z) = (5, 25, 5)$ (which is similar to a dawnside point in a STORM orbit). Each satellite's field of view is the same, and is directed toward the point $(x, y, z) = (7, 0, 0)\,R_E$, close to the subsolar location of the magnetopause. Panel a of Figure 3 is an XZ plane cut for $Y = 0$ through the reconstruction volume; panel b is an XY plane cut for $Z = 0$. The colored curves in panels c and d are the emissions along the correspondingly colored lines in the panels above. For panel c the blue, green, and red curves thus correspond to $Z = 0$, $Z = 4$, and $Z = 5$, respectively, while for panel d they correspond to $Y = -3$, $Y = 4$, and $Y = 5$. In panels c and d the solid curves are from the reconstructions in panels a and b; the superimposed dashed curves are derived from the true emissions given in Figure 1.

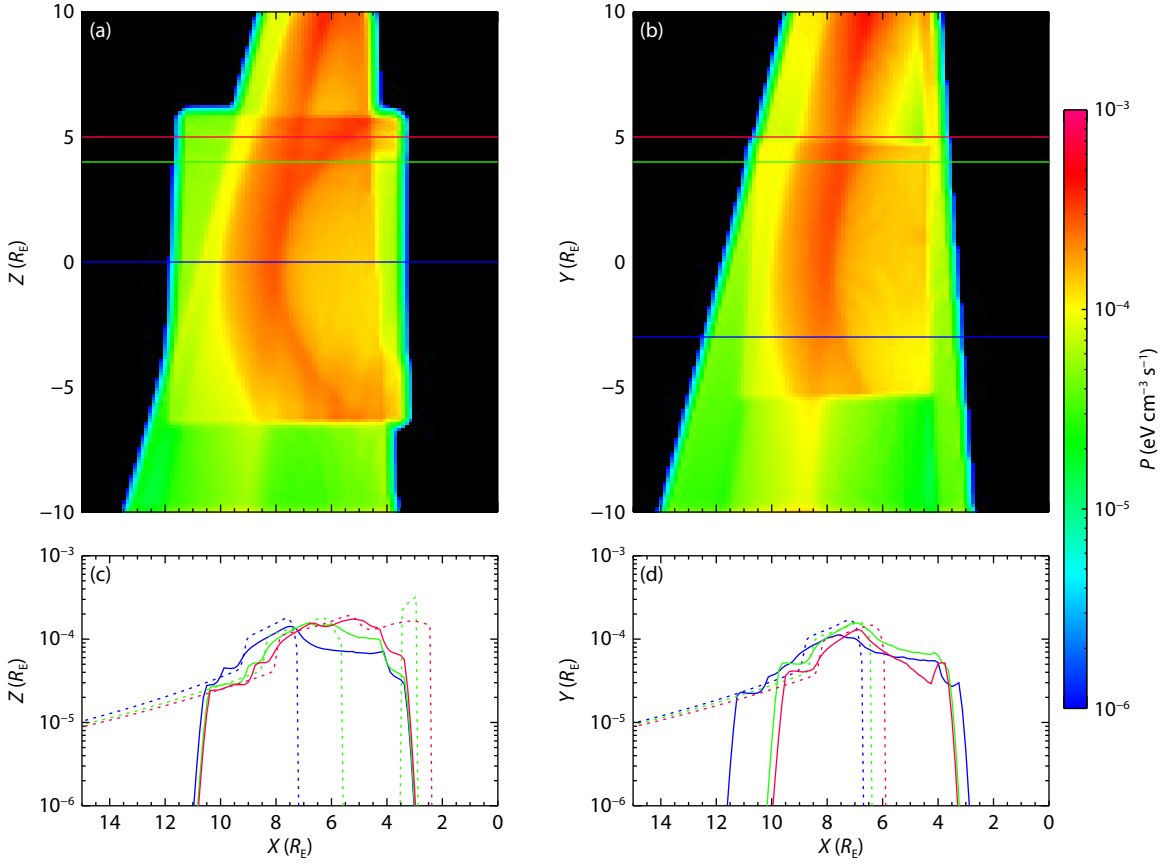

Figure 3. Reconstruction based on two images, a, and b, recorded from satellites at $(x, y, z) = (5, 5, 20)$, and $(x, y, z) = (5, 25, 5)$, respectively. Panel a is an XZ cut for $Y = 0$ through the reconstruction; panel b is an XY cut for $Z = 0$. Panels c and d show profiles corresponding to the same colored lines in the panels above, $Z = 0$ for blue, $Z = 4$ for green, and $Z = 5$ for red in panel c; $Y = -3$ for blue, $Y = 4$ for green, and $Y = 5$ for red in panel d. In panels c and d the solid curves are cuts through the reconstruction while the dashed curves are cuts through the true emissions, given in Figure 1.

Figures 3 through 7 have identical layouts.

The reconstruction can be improved with more images or by adding constraints. For example, the reconstruction with symmetry (case B), shown in Figure 4, adds the constraint that the magnetosheath should be mirror-symmetric around an axis (we choose the *X*-axis); this is equivalent to doing the reconstruction with four images, the additional two being recorded from the mirror points of the real images, $(x, y, z) = (5, -5, -20)$, and $(x, y, z) = (5, -25, -5)$. These two additional images are identical to images a and b except for being mirrored, so we do not show them separately. It is immediately clear that case B provides a significantly better reconstruction along the *X*-axis (blue curve in panel c), as well as a much improved reconstruction for $(y, z) = (-3, 0)$ (blue curve in panel d).

3.2 Three Satellites

We perform two different reconstructions using images from three satellites. The first, case C, presented in Figure 5, uses images a, b, and c, recorded, respectively, from vantage points $(x, y, z) = (5, 5, 20)$, $(x, y, z) = (5, 25, 5)$, and $(x, y, z) = (5, -25, 5)$. These images are recorded largely from the *YZ* plane; all contain a sharp edge related to the magnetopause. This reconstruction is significantly better than the two-satellite reconstruction, comparable even to the two-satellites reconstruction with symmetry.

But if we look at a different set of three vantage points, which we will call case D, presented in Figure 6, the reconstruction is not as good. Here we use images a, b, and d, recorded from $(x, y, z) = (5, 5, 20)$, $(x, y, z) = (5, 25, 5)$, $(x, y, z) = (55, 10, -5)$, the third satellite observing from the dayside (Figure 2d). A significant difference between the first two images and the third image is that the third images does not contain the sharp boundaries of the dayside magnetopause. That image observes through the magnetosheath at a pependicular angle to most of it, and thus does not contain much information about the location of the boundary. This lack of boundary information results in a worse reconstruction than the other three-image reconstruction, case C. The third image of case D also covers a larger area across the magnetosheath, resulting in, effectively, two-image reconstruction in the periphery of the reconstruction volume. It can even be argued that in some regions (e.g. negative *Y*), the case D reconstruction is worse than just using the two images a and b.

3.3 Four Satellites

For the reconstruction with four satellites, case E, we use images a, b, e, and f, recorded, respectively, at $(x, y, z) = (5, 5, 20)$, $(x, y, z) = (5, 25, 5)$, $(x, y, z) = (25, 25, 9)$, and $(x, y, z) = (17, 17, 17)$. This reconstruction is better than all the others, with the possible exception of case B, in terms of the spatial distribution of emissions but not better in terms of determining the location of the subsolar point on the magnetopause.

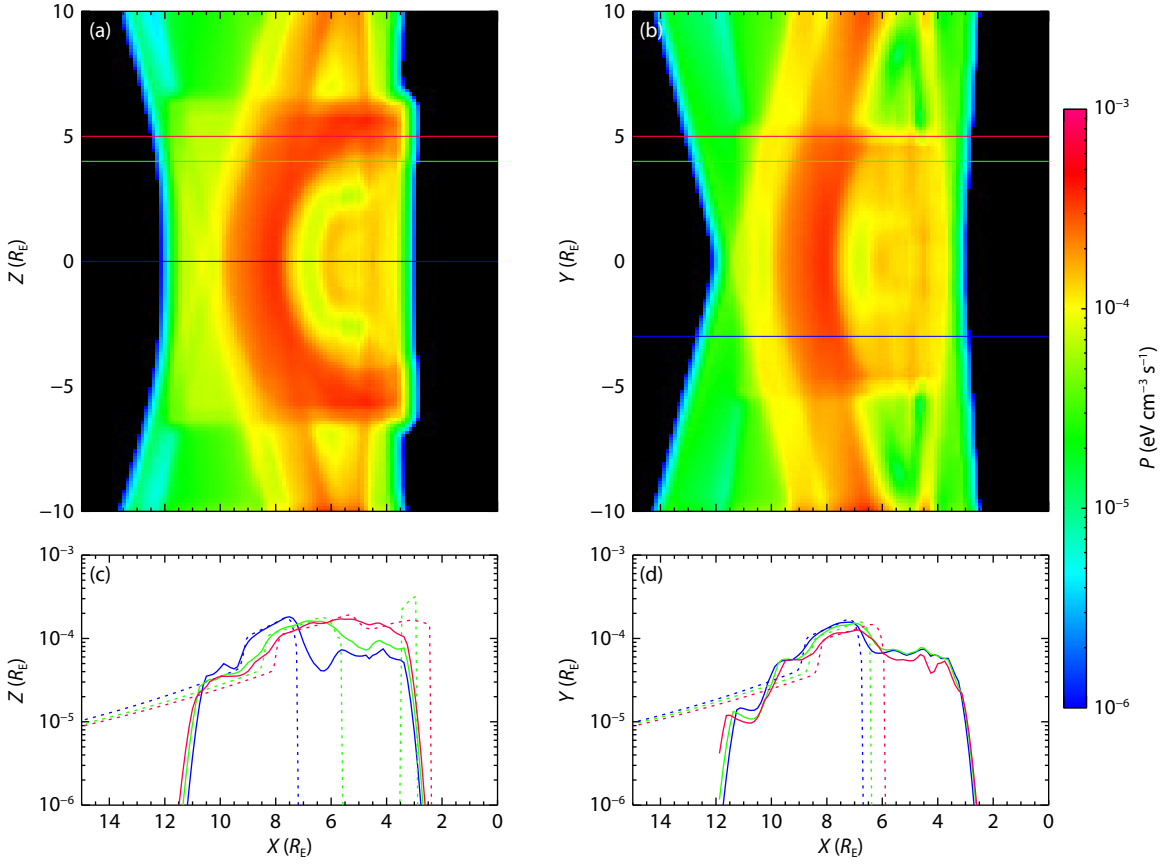

Figure 4. Reconstruction based on the two satellite images, a and b, using symmetry, which results, effectively, in using images from four locations, $(x, y, z) = (5, 5, 20)$, $(x, y, z) = (5, 25, 5)$, and their symmetric locations $(x, y, z) = (5, -5, -20)$, and $(x, y, z) = (5, -25, -5)$. See Figure 3 caption for description details.

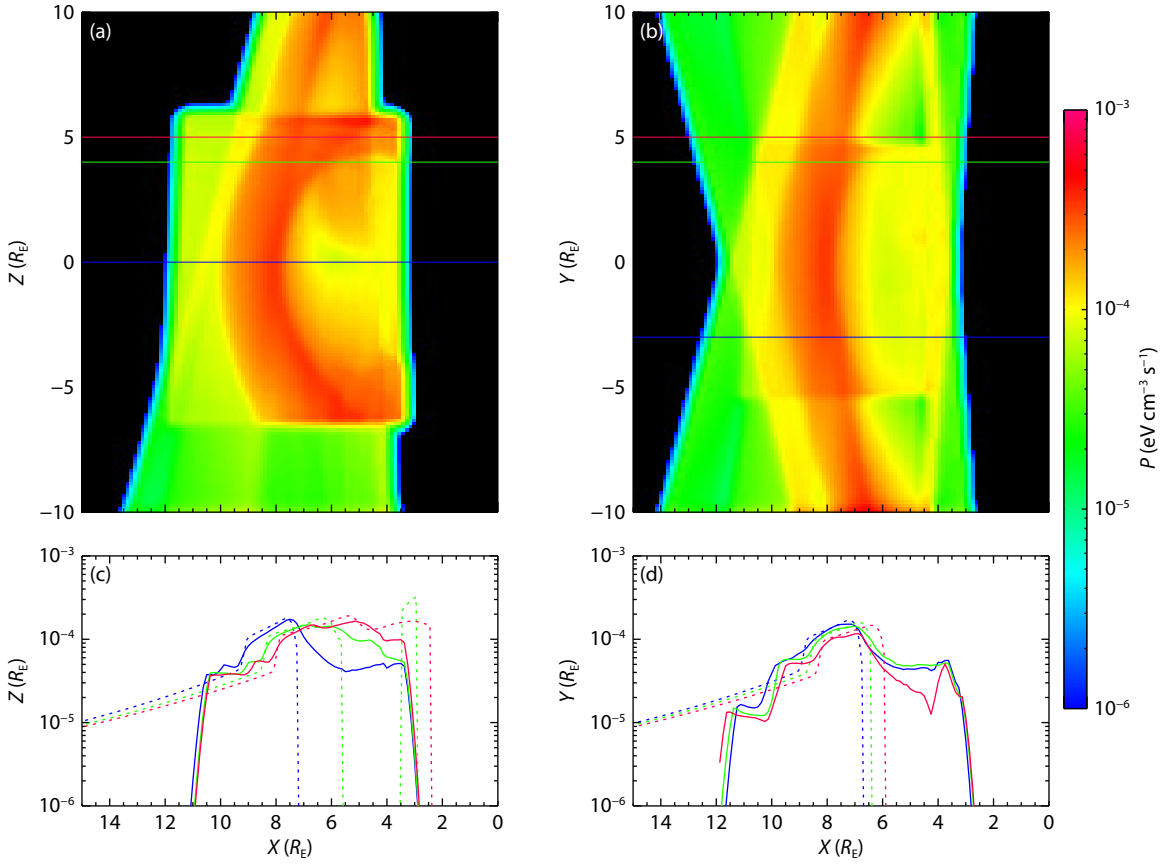

Figure 5. Reconstruction based on three satellites, first configuration, using images a, b, and c recorded from locations $(x, y, z) = (5, 5, 20)$, $(x, y, z) = (5, 25, 5)$, and $(x, y, z) = (5, -25, 5)$. See Figure 3 caption for description details.

4. Discussion

The first thing to note is the obvious one, that, generally, the reconstructions are more accurate when more images are used. This very obvious conclusion does, however, ignore some details. For example, if we look at the two reconstructions using three images, the reconstruction using images, a, b, and c is better than the reconstruction using images a, b, and d. Image d does not contribute meaningfully to the reconstruction of the magnetosheath, or to the location of the magnetopause near the subsolar point. Also, it appears that the reconstruction with two images with symmetry (thus effectively four images), is more accurate than the reconstruction with a separate set of four images. Thus, the geometry matters.

Another important consideration is the fact that, in general, the images from different satellites do not observe the same object. In the present case the magnetosheath extends beyond the fields-of-view of the different images. If the different images' fields-of-view do not overlap exactly, which they cannot possibly do in these fan-shaped fields-of-view, then they will see different objects. The ART algorithm assumes that all images used in the reconstruction see the same object, and the complete object. Or, more precisely, that all the pixels in all the images provide uniform coverage of the object. This is generally fulfilled in medical imaging in which a camera, sometimes consisting of an X-ray emitter and an image plane, rotates around the body being imaged. But even in medical imaging the coverage is not always complete; the resulting artifacts in the reconstruction are called truncation artifacts (Mawlawi et al., 2006). That paper discusses an approach to reducing truncation artifacts by introducing a model of the portion of the body that extends beyond the FOV of some scans. We believe this approach is also potentially viable for future tomographic reconstruction of space imaging, one which we intend to investigate.

In our modeling efforts, and in tomographic reconstruction in general using a few spacecraft, the requirement of uniform coverage will practically never be fulfilled. If we look at images a, b, and d, which are the basis of the reconstructions in Figure 6, we see that three different observable fields of view are involved. The dayside satellite covers most of the reconstruction volume in the equatorial plane (Figure 6b), whereas the other two satellites each cover a smaller volume. The volume covered by image a can be seen in Figure 6b as an approximately rectangular shape. Similarly, the volume covered by image b can be seen as an approximately rectangular shape in Figure 6a. Outside of the common volume of images a and b, some of the volume is covered by two images, and some by just one image. In the parts of the volume covered by only one image, the reconstructed emission will be close to constant along the rays. In Figure 6b that is the area to the left and right of the fan that spans 10 to 4 R_E at the top, and 14 to 3 R_E at the bottom. The top and bottom of that fan are also regions covered by only one image. The emissions in those regions will tend to be emissions that the algorithm cannot place anywhere else. One way to eliminate these effects is to reduce the

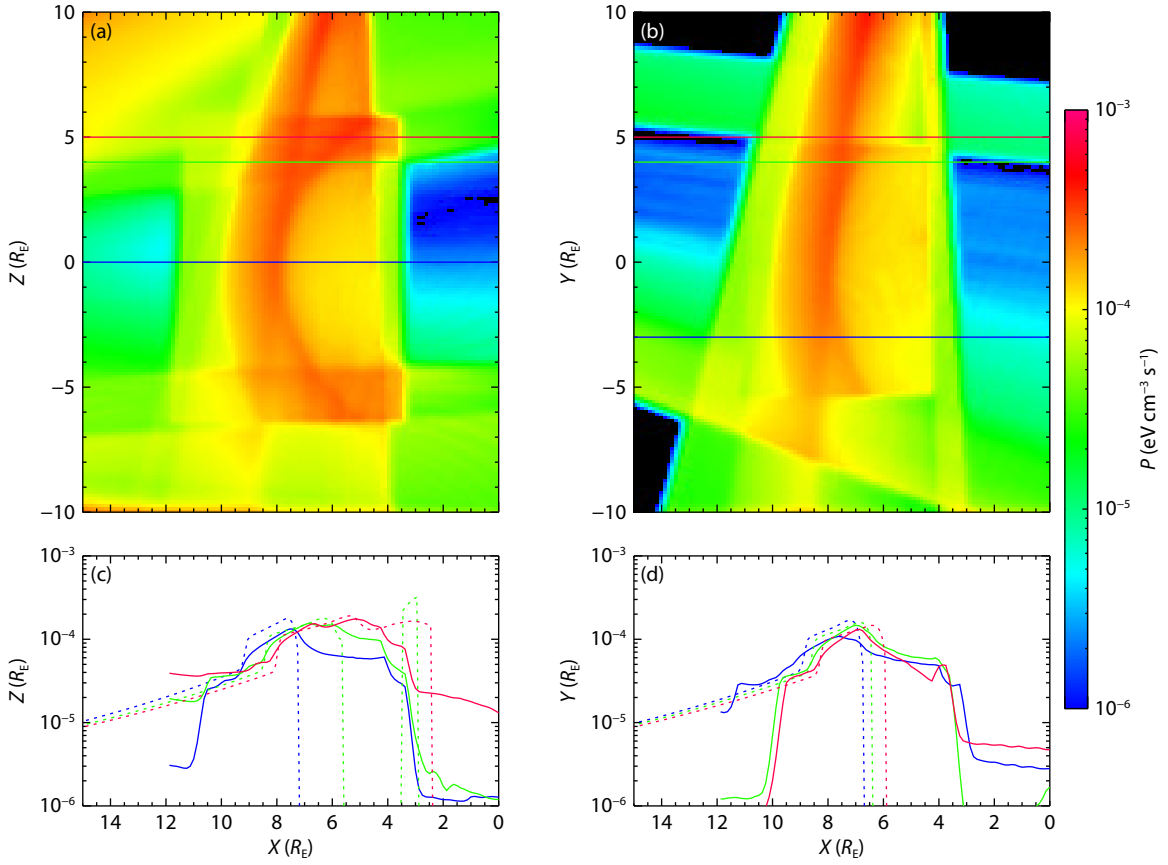

Figure 6. Reconstruction based on three satellites, second configuration, using images a, b, and d, recorded from $(x, y, z) = (5, 5, 20)$, $(x, y, z) = (5, 25, 5)$, and $(x, y, z) = (55, 20, -5)$. See Figure 3 caption for description details.

size of the reconstruction volume, thus forcing more emission into the core region covered by all three images. While that can help some, it is problematic when the images don't see the same object. For example, again referring to Figure 6b, image b, which forms the fan in this plane, observes portions of the magnetosheath that are not contained in image a (portions that are dawnward and duskward of the field-of-view of image a), and thus restricting the reconstruction volume to a volume covered only by image a, will not result in a correct reconstruction either. Nonetheless, experience shows us that manipulation of the geometry of the dimensions of the reconstruction volume is one of the regularization tools that can be used to improve a reconstruction in this sort of under-constrained problem.

Despite all of these difficulties we are able to get good accuracy of reconstruction of the magnetopause boundary. Even using just two images, the reconstructed magnetopause boundary is less than 0.5 R_E different (which is the science requirement for the SMILE mission) from the true location of the boundary at the subsolar point, when the peak emission is used as the proxy for the boundary location (compare the solid and dashed blue traces in Figure 3c). As more images are added, that difference decreases a little, but the primary improvement is that the reconstructed location of the boundary is captured more accurately away from the subsolar point as well. However, adding images should be done judiciously, as we saw in Figure 6, where adding an image resulted in no improvement, and possibly even a less accurate reconstruction. However, including other constraints, such as symmetry, can improve the accuracy of the reconstruction. In fact, the reconstruction in Figure 4, using two images plus a symmetry constraint, results in a reconstruction accuracy that is similar to what we obtained with four images (Figure 7). Using four images improves the reconstruction of the emission in the magnetosheath, but results in no, or modest, improvement in the accuracy of the reconstructed position of the subsolar point on the magnetopause.

For a more quantitative comparison we have computed some quality measures which are listed in Table 1. The five rows of the table refer to the five reconstruction cases which are also labeled with letters A through E. r_{MP} is the position of the subsolar point on the magnetopause computed from the reconstruction. It is computed as the point along the X-axis where the reconstructed emission is maximum. By comparison, the true value is 7.65 R_E, and with a grid spacing of 0.125 R_E all the reconstructions produce the correct value. Next are three sections in the table, for which three measures are computed for a region around the X-axis. The first section for a region within 0.1 R_E from the X-axis, and the other two sections for regions within 1 R_E and 3 R_E, from the X-axis, respectively. In each region we compute three measures, δ_{MP}, σ_{MP}, and σ_P. δ_{MP} is the average difference between the position of the magnetopause as measured in the real data and in the reconstructed volume. The position of the magnetopause is obtained as the location of maximum emission. The second measure is the

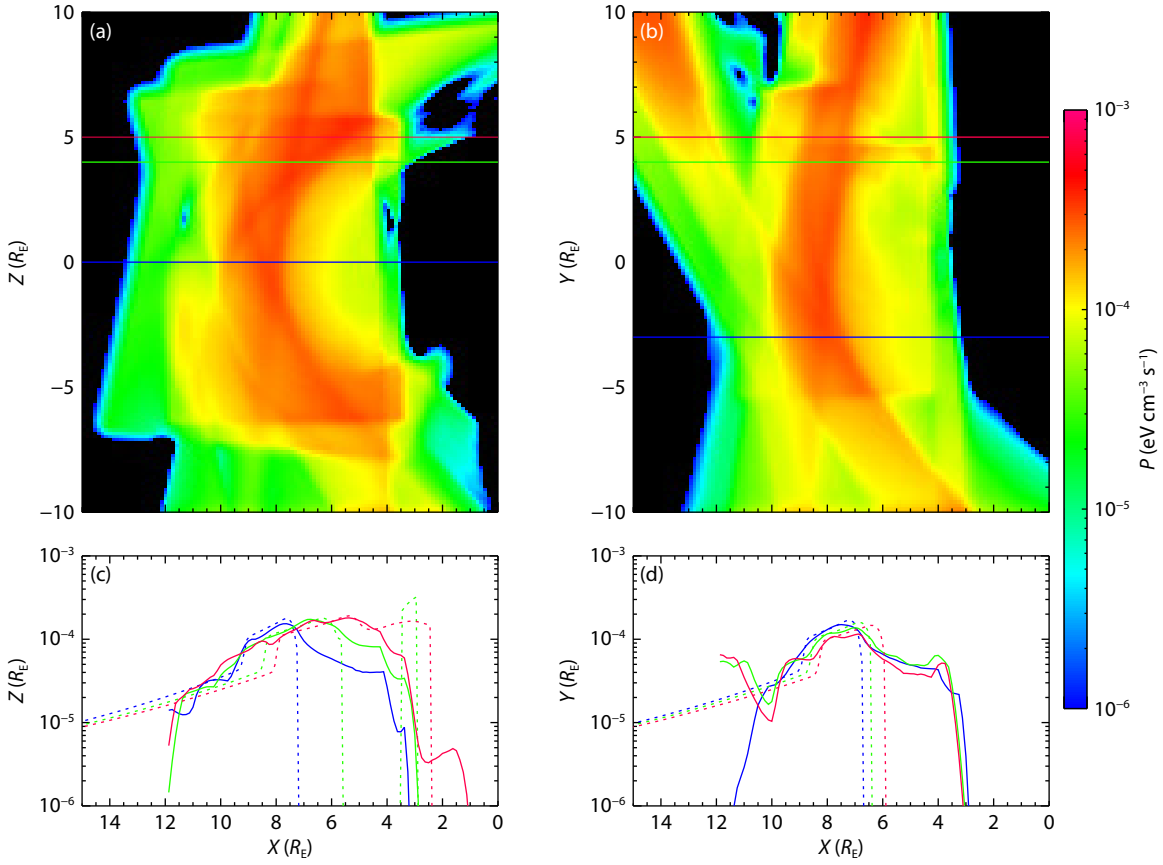

Figure 7. Reconstruction based on four satellites, using images a, b, e, and f, recorded from $(x, y, z) = (5, 5, 20)$, $(x, y, z) = (5, 25, 5)$, $(x, y, z) = (25, 25, -9)$, and $(x, y, z) = (17, 17, 17)$, respectively. See Figure 3 caption for description details.

Table 1. Quantitative comparison of the reconstructed vs. true values for each of the five reconstruction cases. The measures δ_{MP}, σ_{MP}, and σ_P are described in detail in the text.

		$R < 0.1\ R_E$			$R < 1\ R_E$			$R < 3\ R_E$		
Exp.	r_{MP}	δ_{MP}	σ_{MP}	σ_P	δ_{MP}	σ_{MP}	σ_P	δ_{MP}	σ_{MP}	σ_P
A	7.6	−0.09	0.09	31	−0.10	0.12	31	0.002	0.18	29
B	7.6	−0.09	0.09	3.9	−0.04	0.06	3.9	0.04	0.11	5.5
C	7.6	−0.09	0.09	13	−0.07	0.09	13	0.01	0.12	11
D	7.6	−0.09	0.09	41	−0.09	0.12	41	0.003	0.18	38
E	7.8	0.13	0.14	14	0.05	0.15	15	0.11	0.25	16

σ_{MP}, which is the RMS difference of the same two positions. The third measure, σ_P is the RMS difference between the true and the reconstructed emission in the magnetosheath, in the units of the line plots, multiplied by 10^6. The magnetosheath is bounded by the magnetopause and the bow shock. The bow shock is determined as the location of the steepest negative gradient of the emission in the true emission. The magnetosheath then spans of the order of 2 R_E.

The results in the table are interesting. First we note that there is, for the most part, a modest increase in the error of the reconstruction of the magnetopause position, σ_{MP}, when one examines a progressively larger region around the X-axis, e.g. from ($R < 0.1\ R_E$) to ($R < 3\ R_E$). Second, we note the differences in the accuracy of the reconstructed emission, σ_P . There it is interesting that by far the best reconstruction is in case B, two images with symmetry, thus effectively four images symmetrically located. For four images not symmetrically located (case E) the reconstruction is less accurate, and for the two different cases of reconstruction with three images, case C is better than case D. Case D uses imaged which does not provide much information about the magnetopause location, whereas in case C all three images contribute.

Although this paper is not an exhaustive exploration of geometries it is clear that some geometries will not produce a good reconstruction even when the satellites are widely spaced in angle and observe the same parts of the magnetosheath. An image that observes the boundary orthogonally does not contain much information about the distance to that boundary. As an example,

consider a polar satellite (similar to the SMILE mission), and an equatorial satellite (similar to the STORM mission). When the equatorial satellite is on the dayside (or the nightside, assuming it can observe in the direction of the sun), the equatorial satellite may be imaging the magnetosheath but only see a more-or-less uniform emission. When that observation is used in conjunction with a polar satellite image the result will be emission distributed more-or-less uniformly along the look directions of the individual pixels in the polar satellite image. That then means that, to provide useful data for reconstruction, the equatorial satellite needs to be near dawn or dusk while the polar satellite is over the pole. Without careful orbit planning this can significantly limit the number of useful reconstructions from a equatorial/polar mission.

5. Conclusion

In this paper we have shown that it is possible to reconstruct the location of the subsolar point on the magnetopause from just two soft X-ray images. This is important because it allows for instantaneous monitoring of the magnetopause positions using two satellites. With more images, from three or four satellites, it is possible reconstruct also the shape of the magnetopause near the subsolar region, as well as the emission from the magnetosheath, if those three or more satellites are positioned advantageously. For three satellites we showed an example of a good placement of the satellites, as well as a not-so-good placement of the satellites, with the not-so-good placement providing no improvement, and possibly even a worse reconstruction than using just two satellites, for some aspects of the reconstruction. Images from a dayside vantage point do not contain much information about the location of the magnetopause boundary. For a mission consisting of an equatorial satellite in combination with a polar satellites we thus expect that reconstructions will not work as well when the equatorial satellite is on the dayside.

Acknowledgments

The authors gratefully acknowledge Prof. Y. Q. Hu for providing information on the MHD simulation code. This work was supported by NNSFC grants 42322408, 42188101and 42074202; the Strategic Pioneer Program on Space Science, CAS Grant nos. XDA15350201, and in part by the Research Fund from the Chinese Academy of Sciences and the Specialized Research Fund for State Key Laboratories of China. Tianran Sun is also supported by the Young Elite Scientists Sponsorship Program (CAST-Y20 2045).

References

Akasofu, S. I. (1964). The development of the auroral substorm. *Planet. Space Sci.*, *12*(4), 273–282. https://doi.org/10.1016/0032-0633(64)90151-5

Aso, T., Ejiri, M., Urashima, A., Miyaoka, H., Steen, Å., Brändström, U., and Gustavsson, B. (1998). First results of auroral tomography from ALIS-Japan multi-station observations in march, 1995. *Earth, Planets Space, 50*(1), 81–86. https://doi.org/10.1186/BF03352088

Branduardi-Raymont, G., Wang, C., Escoubet, C. P., Adamovic, M., Agnolon, D., Berthomier, M., Carter, J. A., Chen, W., Colangeli, L., … Zhu, Z. (2018). SMILE definition study report. European Space Agency.

Brittnacher, M., Spann, J., Parks, G., and Germany, G. (1997). Auroral observations by the polar ultraviolet imager (UVI). *Adv. Space Res.*, *20*(4-5), 1037–1042. https://doi.org/10.1016/S0273-1177(97)00558-9

C:son Brandt, P., Demajistre, R., Roelof, E. C., Ohtani, S., Mitchell, D. G., and Mende, S. (2002). Image/high-energy energetic neutral atom: global energetic neutral atom imaging of the plasma sheet and ring current during substorms. *J. Geophys. Res.: Space Phys.*, *107*(A12), 1454. https://doi.org/10.1029/2002JA009307

Carter, J. A., Sembay, S., and Read, A. M. (2010). A high charge state coronal mass ejection seen through solar wind charge exchange emission as detected by XMM-Newton. *Mon. Not. Roy. Astron. Soc.*, *402*(2), 867–878. https://doi.org/10.1111/j.1365-2966.2009.15985.x

Chambolle, A. (2004). An algorithm for total variation minimization and applications. *J. Math. Imaging Vis.*, *20*(1-2), 89–97. https://doi.org/10.1023/B:JMIV.0000011325.36760.1e

Cravens, T. E. (2000). Heliospheric X-ray emission associated with charge transfer of the solar wind with interstellar neutrals. *Astrophys. J. Lett.*, *532*(2), L153. https://doi.org/10.1086/312574

Ezoe, Y., Funase, R., Nagata, H., Miyoshi, Y., Nakajima, H., Mitsuishi, I., Ishikawa, K., Numazawa, M., Kawabata, Y., … Kashiwakura, K. (2023). GEOspace X-ray imager (GEO-X). *J. Astron. Telesc., Instrum., Syst.*, *9*(3), 034006. https://doi.org/10.1117/1.JATIS.9.3.034006

Gordon, R., Bender, R., and Herman, G. T. (1970). Algebraic reconstruction techniques (ART) for three-dimensional electron microscopy and X-ray photography. *J. Theor. Biol.*, *29*(3), 471–481. https://doi.org/10.1016/0022-5193(70)90109-8

Guo, Y. H., Wang, C., Wei, F., Sun, T. R., Yu, X. Z., Peng, S. W., Branduardi-Raymont, G., and Sembay, S. (2021). A lunar-based soft X-ray imager (LSXI) for the Earth's magnetosphere. *Sci. China Earth Sci.*, *64*(7), 1026–1035. https://doi.org/10.1007/s11430-020-9792-5

Gustavsson, B. (1998). Tomographic inversion for ALIS noise and resolution. *J. Geophys. Res.: Space Phys.*, *103*(A11), 26621–26632. https://doi.org/10.1029/98JA00678

He, H., Shen, C., Wang, H. N., Zhang, X. X., Chen, B., Yan, J., Zou, Y. L., Jorgensen, A. M., He, F., … Xu, R. L. (2016). Response of plasmaspheric configuration to substorms revealed by Chang'e 3. *Sci. Rep.*, *6*(1), 32362. https://doi.org/10.1038/srep32362

Henderson, M. G., Reeves, G. D., Spence, H. E., Sheldon, R. B., Jorgensen, A. M., Blake, J. B., and Fennell, J. F. (1997). First energetic neutral atom images from Polar. *Geophys. Res. Lett.*, *24*(10), 1167–1170. https://doi.org/10.1029/97GL01162

Henderson, M. G., Reeves, G. D., Moore, K. R., Spence, H. E., Jorgensen, A. M., Fennell, J. F., Blake, J. B., and Roelof, E. C. (1999). Energetic neutral atom imaging with the polar ceppad/ips instrument: initial forward modeling results. *Phys. Chem. Earth, Part C: Sol., Terr. Planet. Sci.*, *24*(1-3), 203–208. https://doi.org/10.1016/S1464-1917(98)00029-4

Hu, Y. Q., Guo, X. C., and Wang, C. (2007). On the ionospheric and reconnection potentials of the earth: results from global MHD simulations. *J. Geophys. Res.: Space Phys.*, *112*(A7), A07215. https://doi.org/10.1029/2006JA012145

Huang, Y., Dai, L., Wang, C., Xu, R. L., and Li, L. (2021). A new inversion method for reconstruction of plasmaspheric He^+ density from EUV images. *Earth Planet. Phys.*, *5*(2), 218–222. https://doi.org/10.26464/epp2021020

Jorgensen, A. M., Sun, T. R., Wang, C., Dai, L., Sembay, S., Zheng, J. H., and Yu, X. Z. (2019). Boundary detection in three dimensions with application to the SMILE mission: the effect of model-fitting noise. *J. Geophys. Res.: Space Phys.*, *124*(6), 4341–4355. https://doi.org/10.1029/2018JA026124

Jorgensen, A. M., Kepko, L., Henderson, M. G., Spence, H. E., Reeves, G. D., Sigwarth, J. B., and Frank, L. A. (2000). Association of energetic neutral atom bursts and magnetospheric substorms. *J. Geophys. Res.: Space Phys.*, *105*(A8), 18753–18763. https://doi.org/10.1029/1999JA000445

Jorgensen, A. M., Xu, R., Sun, T., Huang, Y., Li, L., Dai, L., and Wang, C. (2022). A theoretical study of the tomographic reconstruction of magnetosheath X-ray emissions. *J. Geophys. Res.: Space Phys.*, *127*(4), e2021JA029948. https://doi.org/10.1029/2021JA029948

Mawlawi, O., Erasmus, J. J., Pan, T., Cody, D. D., Campbell, R., Lonn, A. H., Kohlmyer, S., Macapinlac, H. A., and Podoloff, D. A. (2006). Truncation artifact on PET/CT: impact on measurements of activity concentration and assessment of a correction algorithm. *Am. J. Roentgenol.*, *186*(5), 1458–1467. https://doi.org/10.2214/AJR.05.0255

Mende, S. B., Harris, S. E., Frey, H. U., Angelopoulos, V., Russell, C. T., Donovan, E., Jackel, B., Greffen, M., and Peticolas, L. M. (2008). The THEMIS array of

ground-based observatories for the study of auroral substorms. *Space Sci. Rev.*, *141*(1), 357–387. https://doi.org/10.1007/s11214-008-9380-x

Owens, M. J., Lockwood, M., Barnard, L. A., and MacNeil, A. R. (2018). Generation of inverted heliospheric magnetic flux by coronal loop opening and slow solar wind release. *Astrophys. J. Lett.*, *868*(1), L14. https://doi.org/10.3847/2041-8213/aaee82

Paw, U. C. K., Walsh, B., Kuntz, K. D., Nutter, R., Connor, C., Busk, S., Burwitz, V., Hartner, G., Müller, T., … Thomas, N. (2022). X-ray micropore optic array preliminary calibration results for the lunar environment heliospheric x-ray imager. In *Proceedings of SPIE 12181, Space Telescopes and Instrumentation 2022: Ultraviolet to Gamma Ray* (pp. 1162-1185). Montréal, Québec, Canada: SPIE. https://doi.org/10.1117/12.2629503

Roelof, E. C., Mitchell, D. G., and Williams, D. J. (1985). Energetic neutral atoms (*E* ~50 keV) from the ring current: IMP 7/8 and ISEE 1. *J. Geophys. Res.: Space Phys.*, *90*(A11), 10991–11008. https://doi.org/10.1029/JA090iA11p10991

Rudin, L. I., Osher, S., and Fatemi, E. (1992). Nonlinear total variation based noise removal algorithms. *Phys. D: Nonlinear Phenom.*, *60*(1-4), 259–268. https://doi.org/10.1016/0167-2789(92)90242-F

Sandel, B. R., King, R. A., Forrester, W. T., Gallagher, D. L., Broadfoot, A. L., and Curtis, C. C. (2001). Initial results from the IMAGE extreme ultraviolet imager. *Geophys. Res. Lett.*, *28*(8), 1439–1442. https://doi.org/10.1029/2001GL012885

Schwadron, N. A., and Cravens, T. E. (2000). Implications of solar wind composition for cometary X-rays. *Astrophys. J.*, *544*(1), 558–566. https://doi.org/10.1086/317176

Sibeck, D., Murphy, K., Porter, F. S., Walsh, B., Connor, H., Kuntz, K., Zesta, E., Goldstein, J., Frey, H., … Henderson, M. (2023). Imaging the end-to-end dynamics of the global solar wind-magnetosphere interaction. *Bull. Am. Astron. Soc.*, *55*(3). https://doi.org/10.3847/25c2cfeb.9b87eed9

Størmer, C. (1935). Measurements of luminous night clouds in Norway 1933 and 1934. With 3 figures in the text and 17 plates. *Astrophys. Norv.*, *1*, 87.

Sun, T. R., Wang, C., Wei, F., and Sembay, S. (2015). X-ray imaging of Kelvin-Helmholtz waves at the magnetopause. *J. Geophys. Res.: Space Phys.*, *120*(1), 266–275. https://doi.org/10.1002/2014JA020497

Sun, T. R., Wang, C., Sembay, S. F., Lopez, R. E., Escoubet, C. P., Branduardi-Raymont, G., Zheng, J. H., Yu, X. Z., Guo, X. C., … Guo, Y. H. (2019). Soft X-ray imaging of the magnetosheath and cusps under different solar wind conditions: MHD simulations. *J. Geophys. Res.: Space Phys.*, *124*(4), 2435–2450. https://doi.org/10.1029/2018JA026093

Sun, T. R., Wang, C., Connor, H. K., Jorgensen, A. M., and Sembay, S. (2020). Deriving the magnetopause position from the soft X-ray image by using the tangent fitting approach. *J. Geophys. Res.: Space Phys.*, *125*(9), e2020JA028169. https://doi.org/10.1029/2020JA028169

Sun, T. R., Wang, X., and Wang, C. (2021). Tangent directions of the cusp boundary derived from the simulated soft X-Ray image. *J. Geophys. Res.: Space Phys.*, *126*(3), e2020JA028314. https://doi.org/10.1029/2020JA028314

Vallat, C., Dandouras, I., C:son Brandt, P., DeMajistre, R., Mitchell, D. G., Roelof, E. C., Rème, H., Sauvaud, J. A., Kistler, L., … Balogh, A. (2004). First comparisons of local ion measurements in the inner magnetosphere with energetic neutral atom magnetospheric image inversions: Cluster-CIS and IMAGE-HENA observations. *J. Geophys. Res.: Space Phys.*, *109*(A4), A04213. https://doi.org/10.1029/2003JA010224

Wang, C., Li, Z. J., Sun, T. R., Liu, Z. Q., Liu, J., Wu, Q., Zheng, J. H., and Li, J. (2017). SMILE satellite mission survey. *Space Int. (in Chinese)*, *464*(8), 13–16. https://doi.org/10.3969/j.issn.1009-2366.2017.08.003

Wang, C., and Sun, T. R. (2022). Methods to derive the magnetopause from soft X-ray images by the SMILE mission. *Geosci. Lett.*, *9*(1), 30. https://doi.org/10.1186/s40562-022-00240-z